NeuroImage: Clinical 11 (2016) 780–788

Contents lists available at ScienceDirect

NeuroImage: Clinical

journal homepage: www.elsevier.com/locate/ynicl

Non-parametric intravoxel incoherent motion analysis in patients with intracranial lesions: Test-retest reliability and correlation with arterial spin labeling

Sonja Stieb[a,b], Andreas Boss[c], Moritz C. Wurnig[c], Pinar S. Özbay[c,d], Tobias Weiss[e], Matthias Guckenberger[a], Oliver Riesterer[a], Cristina Rossi[c,*]

[a] Department of Radiation Oncology, University Hospital Zurich and University of Zurich, Switzerland
[b] Center for Proton Therapy, Paul Scherrer Institute, Villigen, Switzerland
[c] Institute of Diagnostic and Interventional Radiology, University Hospital Zurich and University of Zurich, Switzerland
[d] Institute for Biomedical Engineering, University of Zurich and ETH Zurich, Switzerland
[e] Department of Neurology, University Hospital Zurich and University of Zurich, Switzerland

ARTICLE INFO

Article history:
Received 7 March 2016
Received in revised form 30 May 2016
Accepted 31 May 2016
Available online 02 June 2016

Keywords:
Intravoxel incoherent motion
IVIM
Arterial spin labeling
ASL
Test-retest reliability
Glioblastoma multiforme

ABSTRACT

Intravoxel incoherent motion (IVIM) analysis of diffusion imaging data provides biomarkers of true passive water diffusion and perfusion properties. A new IVIM algorithm with variable adjustment of the b-value threshold separating diffusion and perfusion effects was applied for cerebral tissue characterization in healthy volunteers, computation of test-retest reliability, correlation with arterial spin labeling, and assessment of applicability in a small cohort of patients with malignant intracranial masses. The main results of this study are threefold: (i) accounting for regional differences in the separation of the perfusion and the diffusion components improves the reliability of the model parameters; (ii) if differences in the b-value threshold are not accounted for, a significant tissue-dependent systematic bias of the IVIM parameters occurs; (iii) accounting for voxel-wise differences in the b-value threshold improves the correlation with CBF measurements in healthy volunteers and patients. The proposed algorithm provides a robust characterization of regional micro-vascularization and cellularity without a priori assumptions on tissue diffusion properties. The glioblastoma multiforme with its inherently high variability of tumor vascularization and tumor cell density may benefit from a non-invasive clinical characterization of diffusion and perfusion properties.

1. Introduction

In spite of aggressive therapy consisting of surgical resection, radiotherapy, and/or chemotherapy, patients with malignant brain tumors have a poor prognosis with a median survival around 8 to 17 months for glioblastoma multiforme (GBM) (Li et al., 2011) and 18 to 31 months for anaplastic astrocytoma (AA) (Paravati et al., 2011). Both tumor types present heterogeneous lesions (Furnari et al., 2007; Yamashita et al., 2016).

The characterization of both, vascularization (Akgoz et al., 2014) and cellularity (Chenevert et al., 2006), of enhancing (Parker et al., 2015) and non-enhancing (Jain et al., 2014) lesions may provide potential prognostic indicators. Pathological alterations of blood flow and volume can be monitored in MRI using both, dynamic contrast enhanced MRI (Piludu et al., 2015) and techniques of arterial spin labeling (ASL) (Jarnum et al., 2010). In addition to perfusion-weighted MRI, the use of diffusion-weighted MRI has been proposed for the quantification of indirect indicators of tumor cell density and cell proliferation (Chenevert et al., 2006).

The intravoxel incoherent motion model in MRI isolates diffusion- and perfusion-related effects on the MR signal attenuation with growing diffusion-weighting of image contrast for increasing *b*-value (Le Bihan et al., 1988). Perfusion-related effects can be detected at low b-values, while further signal attenuation at high b-values is expected to be mainly dominated by diffusion. A few studies have recently investigated the clinical potential of IVIM-indexes for differentiation of brain lesions (Shim et al., 2015), preoperative grading (Hu et al., 2014), or for an assessment of tumor microcirculation (Bisdas et al., 2014). While IVIM promises to yield information on diffusion and microcirculation from a single scan, an important limitation is the robustness of standard fit algorithms, which is jeopardized by the high number of fit parameters and, for most algorithms, by an a priori separation of the perfusion and the diffusion components, with a fixed b-value threshold

* Corresponding author at: Department of Diagnostic and Interventional Radiology, University Hospital Zurich and University of Zurich, Raemistrasse 100, CH-8091 Zurich, Switzerland.
E-mail address: cristina.rossi@usz.ch (C. Rossi).

http://dx.doi.org/10.1016/j.nicl.2016.05.022

(Wurnig et al., 2015). The use of fixed-threshold multi-step algorithms for IVIM has been proposed in the attempt to improve the stability of the multi-parametrical fit (Luciani et al., 2008). Only few studies focused on the dependence of the IVIM-indexes from the b-value threshold in the separation of the diffusion and the perfusion components (Wurnig et al., 2015). However, a dependence of the b-value threshold from tissue type, functional state, or from pathological alteration of tissue microcirculation can be hypothesized (Pazahr et al., 2014) and was proven for abdominal organs (Wurnig et al., 2015). A novel algorithm proposed by Wurnig et al. (Wurnig et al., 2015) addressed the issue of the organ-specific adaptation of the b-value threshold with a variable-threshold IVIM algorithm, which determines the optimal b-value threshold for each voxel based on the fit residuals, independent of assumptions regarding the underlying tissue characteristics.

The aims of this study were to: (i) investigate the repeatability of the variable-threshold algorithm for brain tissue in healthy volunteers by test-retest measurements; (ii) to test the validity of the algorithm for the assessment of the perfusion correlates in patients with malignant intracranial lesions by comparison to quantitative ASL perfusion data.

2. Material and methods

2.1. Subjects

Eleven healthy volunteers (4 men, 7 women; mean age ± standard deviation: 31 ± 6 years, range: 24–39 years) and nine patients with malignant intracranial masses (6 men, 3 women; mean age ± standard deviation: 45 ± 14 years, range: 27–73 years) were included in this prospective study. The study was approved by the local ethics committee. All participants gave written informed consent to the MR examination and the scientific evaluation of the data sets. For the patients, a summary of tumor diagnosis and treatment is reported in Table 1.

2.2. MR protocol

All MR data were acquired on a 3 Tesla whole-body scanner (Ingenia, Philips, Best, The Netherlands) with a 15-channel head coil (Philips, Healthcare, Best, The Netherlands) and using the built-in body transmit coil for spin excitation.

For anatomical orientation, a 3D T1-weighted gradient-echo pulse sequence (TR/TE = 4.5 ms/2.0 ms; flip angle = 8°, echo train length 123, TI = 314 ms, sensitivity encoding factor 2) and a driven equilibrium fast spin echo sequence (TR/TE = 3000 ms/80 ms; echo train length 15, sensitivity encoding factor 2) were acquired.

Diffusion-weighted images for IVIM were acquired using an Echo Planar Imaging (EPI) sequence with spin echo diffusion preparation (TR = 1065 ms; TE = 63 ms; water-fat separation bandwidth = 25.9 Hz; bandwidth in EPI readout direction = 2852.7 Hz/px, sensitivity encoding factor 2; halfscan = 0.677; voxel size = 2.20 × 2.20 × 5.00 mm^3; b-values: 0, 10, 20, 40, 80, 160, 320, 640, 1280 s/mm^2, number of averages 4, three orthogonal diffusion-encoding directions). Depending on the anatomy of the subject ten till twelve slices were acquired resulting in slight variations of the TR of the sequence. Spectral Pre-saturation with Inversion Recovery (SPIR) was used for fat signal saturation. Range and distribution of b-values were selected considering the following points: (i) for b-values above 150–200 s/mm^2 the perfusion effects on the quantification of the diffusion estimates are considered negligible in the brain (Le Bihan, 2011); (ii) five measurement points in the low range of b-values (i.e., below 160 s/mm^2) were selected in order to improve the quality of the perfusion estimates (Lemke et al., 2011); (iii) a b-value above 1000 s/mm^2 should minimize the relative root mean square error in the estimation of the diffusion coefficient (Freiman et al., 2012).

Arterial spin labeling was performed using a balanced pseudo-continuous ASL (pCASL) single-shot gradient echo EPI sequence (Aslan et al., 2010). Imaging parameters were the following: voxel size 3.00 × 3.00 × 5.00 mm^3, 10 slices, TR/TE = 3497 ms/12 ms, flip angle = 40°, sensitivity encoding factor 3, post labeling delay = 1465 ms, labeling duration 1650 ms, label gap 20 mm, RF duration = 0.5 ms, pause between RF pulses = 0.5 ms, labeling pulse flip angle = 18°, bandwidth = 2.0 kHz, echo train length = 29, number of control/tagged pairs = 50. A control volume for cerebral blood flow (CBF) quantification was acquired using the same sequence by setting the labeling delay to 2500 ms.

For each healthy subject, data sets for quantification of diffusion and perfusion estimates (using IVIM and ASL models) were acquired twice. Before acquisition of the second trial, subjects were allowed to adjust the position of the own head within the coil. Volumes acquired during the two trials slightly differed in slice positioning and orientation.

For each patient, T1-weighted images (3D gradient-echo sequence, TR/TE = 1700 ms/2.6 ms, TI = 900 ms, flip angle = 9°, voxel size = 0.47 × 0.47 × 0.90 mm^3) acquired after the administration of Gadolinium-DTPA were available from clinical examinations performed immediately before or after the study examination.

2.3. Post-processing and computation of parametrical maps

The IVIM model (Le Bihan et al., 1988) presumes the MR signal attenuation for increasing strength of the diffusion weighting (i.e. for increasing b-values) to depend on diffusion and perfusion according to the following equation (Eq. 1):

$$\frac{S(b)}{S_0} = f_P \cdot exp(-b \cdot D^*) + (1-f_P) \cdot exp(-b \cdot D). \quad (1)$$

In Eq. 1, $S(b)$ and S_0 represent the signal intensity for a given b-value and for the b-value set to 0 s/mm^2, respectively. The term f_P (fraction of perfusion) is a dimensionless index (between 0 and 1), which mainly reflects the blood volume (Le Bihan et al., 1988). The pseudo-diffusion D^* (in units of mm^2/s) is a perfusion related component of the signal attenuation, which mimics the diffusion process, while D (in units of

Table 1
Summary of patients' data.

Patient	Status*	Gender	Age	Diagnosis	LC (month)	Therapy before MRI	Therapy after MRI
1	Deceased	M	73	GBM	No (5)	Biopsy	6cTMZ, RT, 3× Bevacizumab
2	Deceased	M	32	GBM	No (3)	Operation, RCT, 6cTMZ, bevacizumab	Bevacizumab bevacizumab + CCNU
3	Alive	M	47	AA	No (6)	Operation	RT, operation, 3cTMZ
4	Lost in follow-up	F	55	GBM	No (1)	Biopsy	RT
5	Deceased	F	43	AO	No (5)	Operation, RT, 6cTMZ, bevacizumab	Bevacizumab, RT
6	Alive	M	52	AA	No (3)	Biopsy, 2c TMZ	RT
7	Alive	F	31	AA	No (7)	Operation	RT
8	Alive	M	26	GBM	Yes (7)	Operation	RCT, 3cTMZ
9	Alive	M	50	Met	No (6)	Vandetabib	RT, sorafenib

AA: anaplastic astrocytoma, AO: anaplastic oligodendroglioma, c: cycle, CCNU: lomustine, GBM: glioblastoma multiforme, LC: local control; RCT: radiochemotherapy, RT: radiotherapy, TMZ: temozolomide.

* Status at the time point of the manuscript preparation.

mm^2/s) is the self-diffusion coefficient of water in the tissue. The pseudo-diffusion coefficient is expected to depend on the product between the average blood velocity and the mean capillary segment length, while the f_P is supposed to be proportional to the fractional volume of the capillary blood flowing in each voxel (Le Bihan et al., 1988).

For each b-value, the $S(b)$ was computed by averaging pixel-by-pixel the MR signal acquired along the three diffusion-encoding directions.

Two different algorithms were used for the pixel-wise estimation of the diffusion and perfusion estimates based on Eq. 1.

The first algorithm (hereafter fixed-threshold algorithm) evaluated Eq. 1 in two steps. First, the diffusion coefficient D was estimated by a linear fit of the logarithm of the MR signal attenuation for b-values higher than 160 s/mm^2 (Eq. 2):

$$\ln(S(b)) = -D \cdot b + \ln(S\prime_0), \tag{2}$$

where S'_0 is the intercept of the curve for b = 0 s/mm^2. In a second step, the computed value for D in Eq. 1 was kept constant and f_P and D^* were estimated by a non-linear least-squares Levenberg-Marquardt fit.

The second algorithm (hereafter variable-threshold algorithm) was implemented as proposed in (Wurnig et al., 2015). In this case, optimal diffusion and perfusion estimates were computed using an iterative procedure. Using each of the acquired b-values, from the first to the third-last as threshold value, diffusion and perfusion components were separated and D, D^*, and f_P were computed as following:

(a) D and S'_0 were computed by fitting the logarithm of the signal attenuation to a first degree polynomial curve (Eq. 2) using the above-threshold b-values;
(b) f_P was computed as $f_P = (S_0 - S'_0)/S_0$;
(c) D^* was computed with a non-linear least-squares fit of all signal values by keeping D and f_P fixed.

The steps (a) to (c) were repeated in a loop. The smallest sum of squared residuals in the fitting step (c) was used as a criterion for the identification of optimal D, D^*, f_P, and b-value threshold.

Quantitative CBF maps were computed pixel-wise using the following equation (Eq. 3) (Aslan et al., 2010):

$$CBF = \frac{-\lambda\left(M^{tag} - M^{ctrl}\right)}{2aM_0} \cdot \frac{\exp\left(\delta/T_{1a}\right)}{T_1\left[\exp\left(\frac{\min(\delta - w, 0)}{T_1}\right) - \exp\left(\frac{-w}{T_1}\right)\cdot\left(1 - \frac{T_1 RF}{T_1}\right)\right]}, \tag{3}$$

In the Eq. 3 the parameters represents the following: M^{tag} (M^{ctrl}) is the signal intensity of the tagged (control) image, M_0 is the equilibrium magnetization, $\alpha = 0.86$ is the labeling efficiency, $\lambda = 0.98$ ml/g is the brain-blood partition coefficient, $T_1 = 1.165$ s is the brain tissue longitudinal relaxation time, $T_{1a} = 1.624$ s is the T_1 time of the arterial blood, and $T_{1RF} = 0.75$ s is the T_1 in the presence of off-resonance irradiation. The arterial transit time δ was set to 0.470 ms (Yoshiura et al., 2009).

For each image pair, a CBF map was computed. Before computation of the parametrical maps, the 50 image pairs were realigned to avoid potential detrimental artifacts due to rigid head motion. The reference image volume was also co-registered to the first image volume of the dynamic acquisitions. Realignment and co-registration were performed using the dedicated toolboxes of SPM 12 (Statistical Parametrical Mapping 12, Wellcome Trust Centre for Neuroimaging, London UK). A mean CBF map was obtained as the average of the 50 maps computed using Eq. 3.

All parametrical maps (from Eqs. 1 and 3) were computed using in house custom software written in Matlab (MATLAB Release 2013b, The MathWorks, Inc., Natick, Massachusetts, United States). The computed maps and the morphological images were co-registered using the "fuse-it" tool of PMOD 3.607 (PMOD Technologies Ltd). Image coregistration was performed via reslicing and rigid transformation of the volumes to the morphological image. Reslicing consisted in the adjustment of pixel size and slice thickness of the volume, and was performed by interpolating the image data within oblique planes across the image volume. Rigid transformations rotated and translated the contents of the image volume.

3. Study 1

3.1. Study design

The aim of this part of the study was to investigate the precision of the two algorithms for IVIM maps computation in healthy volunteers. Mean values of the estimated IVIM and ASL parameters were computed over the co-registered segmented gray matter, white matter, and cerebrospinal fluid (CSF) volumes. Segmentation was performed using the "Segment" tool of SPM 12, which relays on a modified gaussian mixture model to assign for the single voxel the probability of belonging to each tissue type (Ashburner et al., 2000). Additionally to the segmented gray matter, RoIs were manually drawn over the morphological volume at the level of the putamen and copied onto the coregistered parametrical maps using the PMOD 3.607 software.

3.2. Histogram analysis

A histogram analysis was performed to quantify the metrics of the perfusion and of the diffusion indexes measured over the segmented tissue types for both IVIM algorithms. Mean value (Av), minimum value (Min), maximum value (Max), standard deviation of the mean value (SD), first and third quartiles (Q1 and Q3), and median (Med) were computed. Single parameters of the histogram metric obtained with the two IVIM algorithms were statistically compared using a paired, two-tailed Student's t-test ($p < 0.05$).

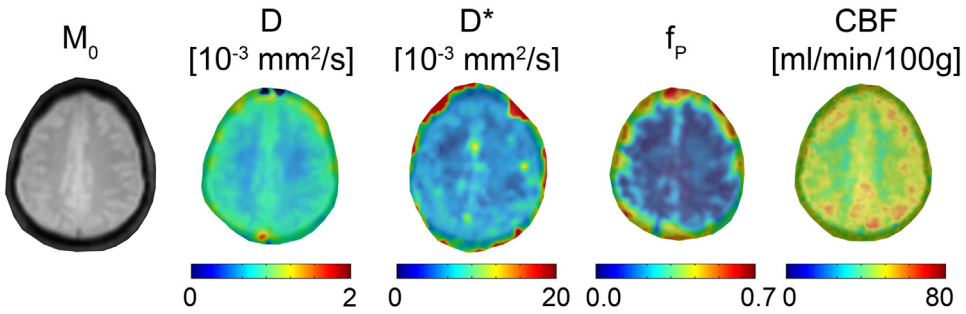

Fig. 1. Cropped M_0 image and parametrical CBF and IVIM maps computed in one healthy volunteer (male, 39 years-old) using the variable threshold algorithm. The computed maps were overlaid onto the M_0-image.

Table 2
Mean values (± standard deviation) of the IVIM indexes computed in both trials (Trial 1: test, Trial 2: retest) using the variable-threshold algorithm and the fixed-threshold algorithm in gray matter, putamen alone, white matter, and cerebrospinal fluid (CSF) in healthy volunteers.

		D [10^{-3} mm^2/s]				D^* [10^{-3} mm^2/s]				f_P			
		Gray matter	Putamen	White matter	CSF	Gray matter	Putamen	White matter	CSF	Gray matter	Putamen	White matter	CSF
Variable-threshold algorithm	Trial 1	0.75 ± 0.03	0.63 ± 0.07	0.66 ± 0.03	0.84 ± 0.08	9.70 ± 1.60	18.1 ± 20.8	8.75 ± 0.99	11.11 ± 3.36	0.15 ± 0.02	0.08 ± 0.04	0.12 ± 0.02	0.28 ± 0.06
	Trial 2	0.75 ± 0.04	0.61 ± 0.04	0.68 ± 0.03	0.88 ± 0.06	9.01 ± 1.16	24.8 ± 23.7	8.75 ± 1.30	11.64 ± 2.54	0.15 ± 0.01	0.08 ± 0.03	0.12 ± 0.01	0.27 ± 0.07
Fixed-threshold algorithm	Trial 1	0.79 ± 0.07	0.66 ± 0.04	0.71 ± 0.03	1.01 ± 1.62	9.88 ± 1.54	47.4 ± 8.2	9.58 ± 1.68	10.07 ± 2.85	0.13 ± 0.02	0.06 ± 0.02	0.09 ± 0.01	0.24 ± 0.09
	Trial 2	0.71 ± 0.28	0.64 ± 0.03	0.71 ± 0.04	1.00 ± 0.15	10.01 ± 1.04	21.5 ± 34.6	9.99 ± 0.93	10.29 ± 2.27	0.12 ± 0.02	0.05 ± 0.02	0.09 ± 0.01	0.24 ± 0.07

3.3. Intra-algorithm repeatability

For each algorithm, test-retest reliability of the mean values (Av) of the diffusion and the perfusion estimates was assessed by computing intra-class correlation coefficients (ICCs) assuming a two-way mixed model for absolute agreement between single measurements (Shrout and Fleiss, 1979). Estimates for ICC were computed using the software SPSS (IBM Corp. Released 2013. IBM SPSS Statistics for Windows, Version 22.0. Armonk, NY: IBM Corp.). The ICCs were classified as (Cicchetti and Sparrow, 1981): excellent above 0.75, good between 0.59 and 0.75, fair between 0.58 and 0.40, and poor for values below 0.40. For each trial coefficients of variation (CV) were computed as the ratio of the standard deviation to the mean.

3.4. Inter-algorithm comparison

For each trial, difference scores between the two measurements were tested using a one-sample t-test ($p < 0.05$).

3.5. Correlation with pCASL

For each of the two algorithms, the strength of the monotonic relationship between CBF and perfusion correlates estimated with the IVIM model (i.e., f_P, D^*, and the product $f_P \cdot D^*$) was measured by computing the Spearman correlation coefficient (r). The correlation was rated as very high for $0.90 < |r| < 1.00$, high for $0.70 < |r| < 0.90$, moderate for $0.50 < |r| < 0.70$, and low for $|r| < 0.50$.

4. Study 2

The aim of this part of the study was to investigate potential advantages of the variable-threshold algorithm in comparison to the fixed-threshold one in the characterization of pathological alteration of diffusion and perfusion estimates in patients with malignant intracranial lesions. Regional CBF, f_P, D^*, and D values were computed in RoIs drawn over the contrast-enhancing lesions, areas of perifocal edema, and necrotic brain tissue. For each patient, parametrical values were also computed over the segmented white matter as a reference. The correlation of the mean IVIM-values to the CBF measurements was tested as in Study 1 by computing the Spearman correlation coefficient. Potential differences in the diffusion and perfusion parameters measured over the single areas were statistically compared using a one-sample t-test ($p < 0.05$).

5. Results

5.1. Study 1

Image quality allowed the computation of IVIM and CBF parametrical maps in all volunteers (Fig. 1). Regional IVIM parameters for both trials are reported in Table 2. The smallest sums of the residuals for the IVIM fits were found at a mean b-value threshold of 281 ± 96 s/mm^2 for the gray matter (Trial 2: 283 ± 80 s/mm^2), and at a mean b-value threshold 362 ± 91 s/mm^2 for the white matter (Trial 2: 364 ± 59 s/mm^2).

5.1.1. Histogram analysis

The results of the histogram analysis are reported in the supplementary material. In summary, differences in the metrics of the diffusion and perfusion estimates between the two algorithms were found in dependence from the tissue type. Generally, an overestimation of the diffusion coefficient D was found using the fixed-threshold algorithm as compared to the variable-threshold algorithm. For gray matter and white matter f_P was underestimated by the fixed-threshold algorithm. For white matter and CSF, the D^* showed a lower reproducibility of the results.

5.1.2. Intra-algorithm repeatability

Both algorithms for IVIM evaluation showed good intra-algorithm patterns (Fig. 2). Mean ICC values were 0.68 ± 0.25 (good) for the variable-threshold algorithm and 0.52 ± 0.35 (fair) for the fixed-threshold algorithm (Table 3). However, for both algorithms the repeatability metrics presented differences between tissue types and diffusion and perfusion parameters. While the repeatability of the estimation of the D coefficient was comparable for both algorithms ($ICC_{variable\text{-}threshold} = 0.51 \pm 0.29$ (fair), $ICC_{fixed\text{-}threshold} = 0.67 \pm 0.29$ (good)), the estimate of D^* was more robust in the case of the variable-threshold algorithm than for the fixed-threshold algorithm ($ICC_{variable\text{-}threshold} = 0.71 \pm 0.27$ (good), $ICC_{fixed\text{-}threshold} = 0.44 \pm 0.43$ (fair)).

5.1.3. Inter-algorithm comparison

Bland-Altman plots (Fig. 3) showed that the diffusion coefficient D computed using the variable-threshold algorithm was systematically lower than the one obtained from the fixed-threshold one, while the

Table 3
Intra-class correlation coefficients (ICCs) were computed to assess intra-algorithm reliability in each tissue type. Coefficients of variation (CVs) are reported as a measure of the distribution of the data points around the mean value for each trial and each algorithm.

		Variable threshold			Fixed threshold		
		ICC	CV trial 1	CV trial 2	ICC	CV trial 1	CV trial 2
GM	D	0.74	0.18	1.01	0.35	0.25	0.49
	D^*	0.42	2.70	3.23	0.08	20.9	22.23
	f_P	0.81	0.61	0.60	0.42	4.76	5.04
WM	D	0.60	0.17	0.24	0.82	0.16	0.18
	D^*	0.77	3.13	3.06	0.32	21.83	11.95
	f_P	0.75	0.54	0.55	0.05	6.72	3.20
CSF	D	0.18	0.41	0.38	0.86	0.28	0.28
	D^*	0.95	1.79	1.81	0.91	17.28	17.25
	f_P	0.95	0.47	0.48	0.88	4.01	1.95

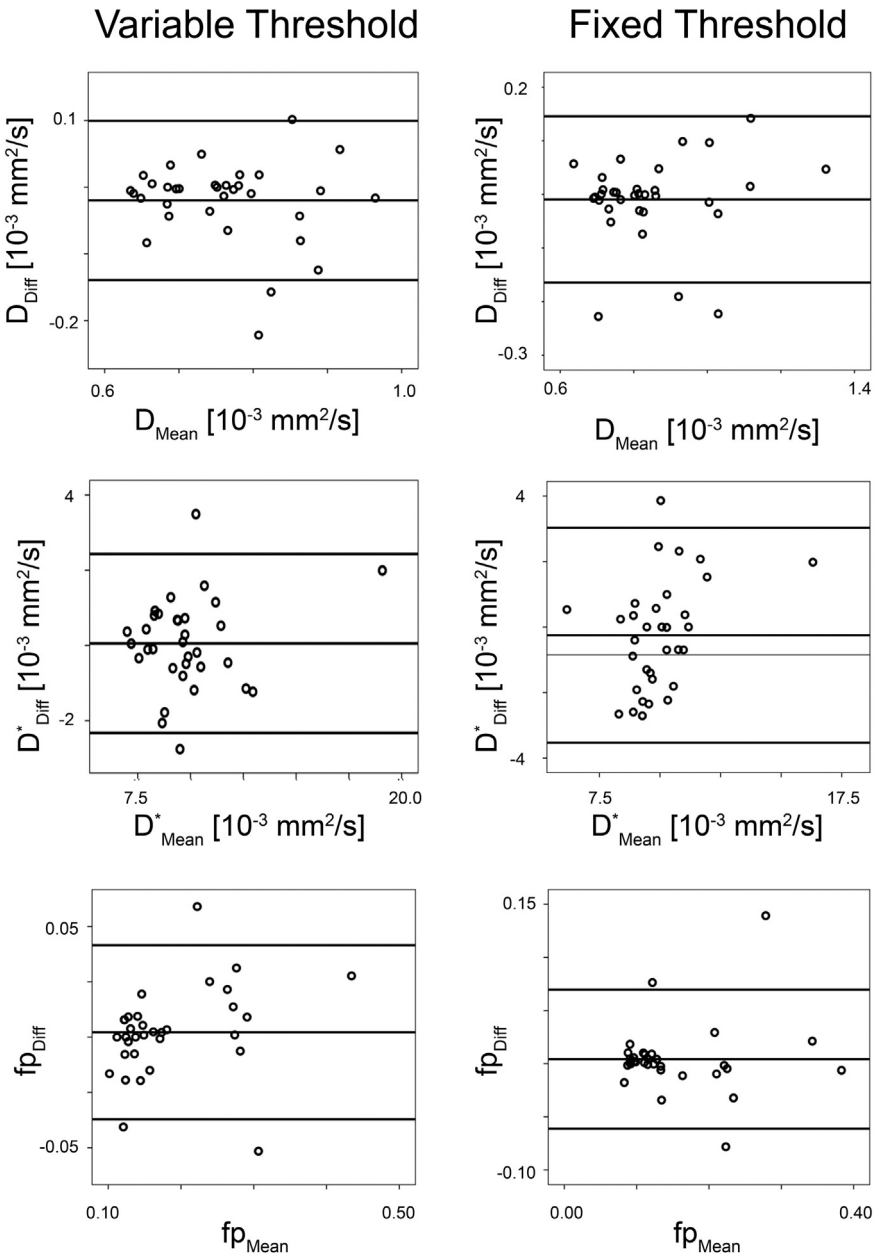

Fig. 2. For each of the reported algorithms, Bland-Altman plots were generated to assess the agreement between the two measurements of the IVIM indexes. For each parameter, the subscript diff refers to the difference between the first and the second trial, while the subscript mean indicates the mean value of the two measurement points.

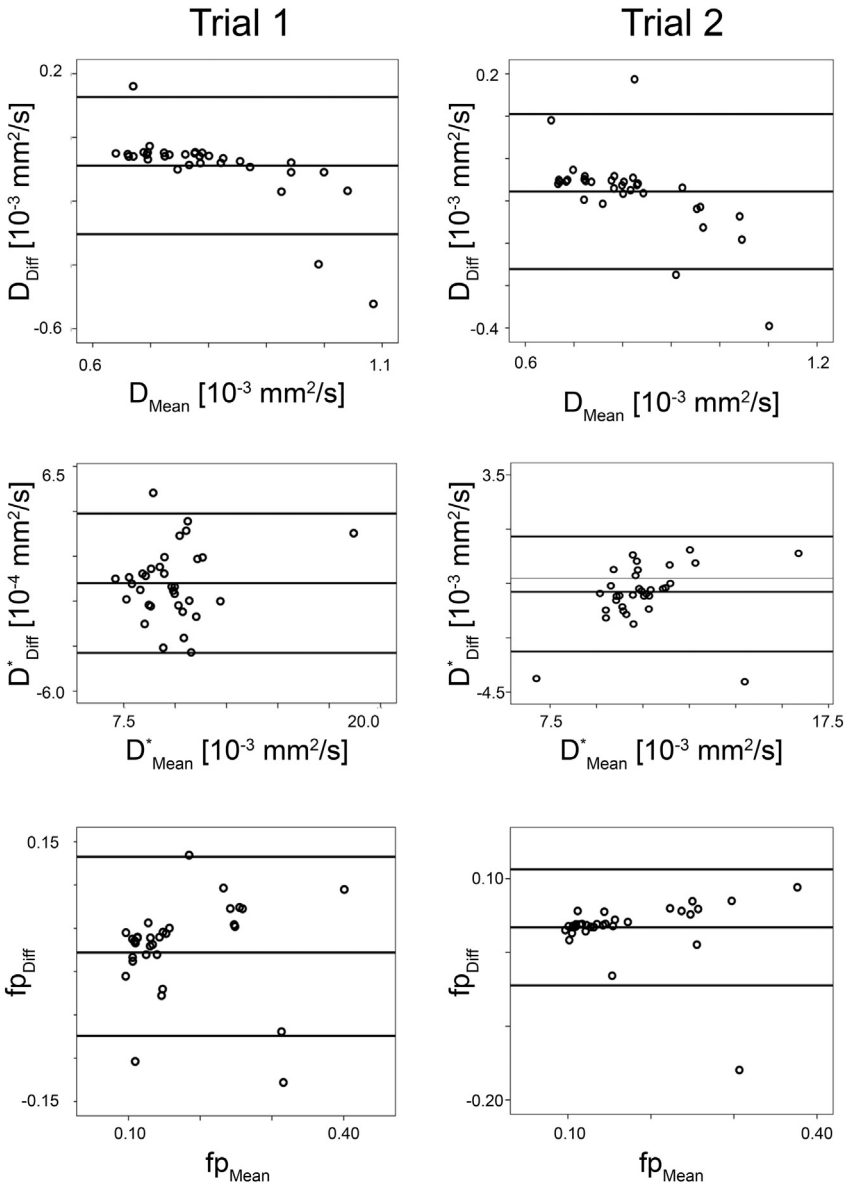

Fig. 3. Inter-algorithm comparison was performed by generating Bland-Altman plots for both trials. The subscript diff refers to the difference between the variable-threshold algorithm and the fixed-threshold one.

f_P was higher than the one assessed with the fixed threshold algorithm. For D and f_P these differences were statistically significant in both, the test and re-test trials ($p < 0.0001$).

5.1.4. Correlation to pCASL

Mean CBF values (in units of ml/min/100 g) for each tissue type were the following: gray matter: 62.3 ± 8.4 (Trial 2, 58.1 ± 1.8); putamen: 52.6 ± 11.8 (Trial 2: 54.3 ± 11.7); white matter: 40.3 ± 1.9 (Trial 2: 43.6 ± 1.8); CSF: 43.6 ± 5.5 (Trial 2: 43.7 ± 2.3). The correlation of IVIM parameters to CBF values varied with tissue type and IVIM-algorithm (Table 4a). For the gray matter, f_P, and $f_P \cdot D^*$ correlated positively with CBF, with the variable-threshold algorithm performing better than the fixed-threshold one in both trials. The putamen showed a high to very high correlation with CBF, with the variable-threshold algorithm performing better than the fixed-threshold one in both trials. A negative correlation between CBF and f_P was measured in the putamen. A

Table 4a
Spearman's correlation coefficients between CBF and IVIM indexes in healthy volunteers. Statistically significant correlation ($p < 0.05$) is highlighted in bold font.

		Gray matter		Putamen		White matter		CSF	
		Trial 1	Trial 2	Trial 1	Trial 2	Trial 1	Trial 2	Trial 1	Trial 2
Variable-threshold algorithm	CBF vs $f_P \cdot D^*$	0.49	0.18	**0.66**	**0.92**	0.20	−0.02	**−0.75**	**−0.68**
	CBF vs f_P	0.42	0.54	**−0.70**	**−0.80**	**0.63**	**0.62**	−0.51	0.15
	CBF vs D^*	−0.18	−0.23	**0.90**	**0.89**	−0.48	−0.24	−0.53	**−0.89**
Fixed-threshold algorithm	CBF vs $f_P \cdot D^*$	0.27	0.17	0.55	**0.79**	0.02	0.36	−0.51	−0.37
	CBF vs f_P	0.20	0.43	−0.57	**−0.64**	0.19	0.57	−0.47	−0.19
	CBF vs D^*	0.18	0.04	0.52	**0.82**	−0.22	−0.08	0.11	−0.45

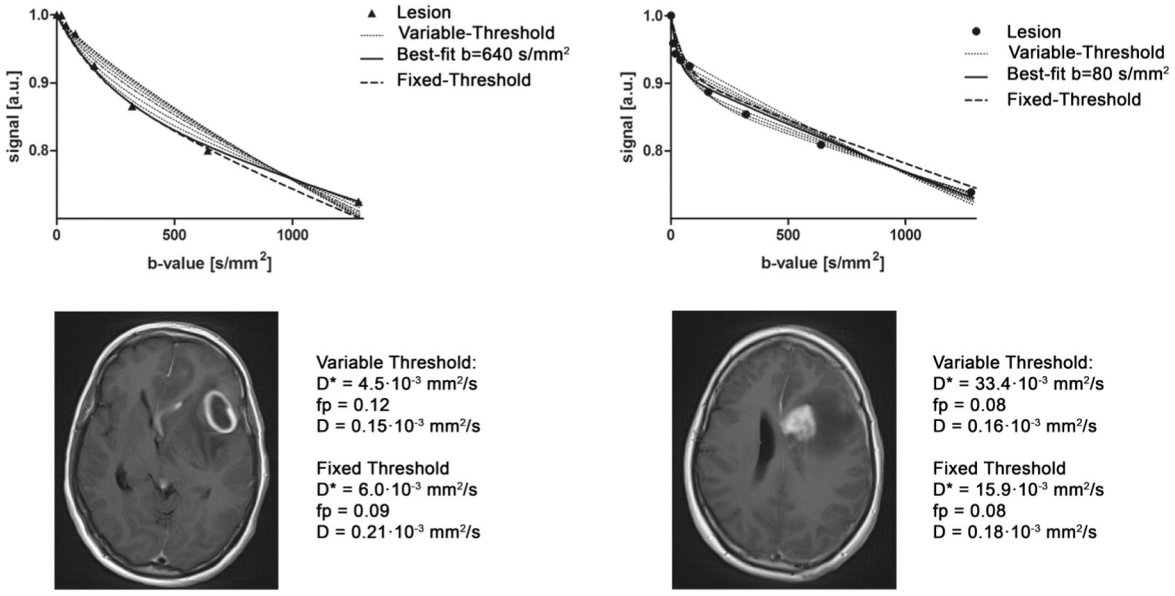

Fig. 4. Curves fitting the signal decay for increasing b-values in a ring-enhancing and in a contrast-enhancing lesion using various b-values as threshold for separation of diffusion and perfusion components. The estimation of the IVIM-indexes depended from the choice of the b-value threshold.

positive moderate correlation was found between f_P, and CBF in the white matter with the variable-threshold algorithm. The same trend was found for the fixed-threshold algorithm, although the correlation was weaker as in the case of the variable-threshold algorithm. Negative correlation between CBF and $f_P \cdot D^*$ was found for the CSF in both algorithms.

5.2. Study 2

For all patients the computed parametrical IVIM maps were of good image quality, based on visual inspection. In two patients pCASL data were not acquired because of delayed time schedule during the routine examination. Regional IVIM values are reported in Table 5.

In patients, a mean CBF of 46.3 ± 9.9 ml/min/100 g was measured over the white matter. Contrast-enhancing lesions showed a mean CBF of 52.6 ± 19.1 ml/min/100 g ($p = 0.45$). Lower CBF values were found over edemas (CBF = 40.7 ± 12.4 ml/min/100 g, $p = 0.37$), while slightly higher CBF values were found over necrotic areas (CBF = 50.0 ± 12.5 ml/min/100 g, $p = 0.56$). For the variable-threshold algorithm, D values measured in the white matter ($0.64 \pm 0.05 \cdot 10^{-3}$ mm²/s) in patients were significantly ($p < 0.001$) lower than the values computed over the lesions ($0.88 \pm 0.14 \cdot 10^{-3}$ mm²/s), edemas ($1.06 \pm 0.19 \cdot 10^{-3}$ mm²/s), and necrotic areas ($0.97 \pm 0.24 \cdot 10^{-3}$ mm²/s). No significant differences were found in the f_P values measured over the white matter (0.12 ± 0.03) as compared to contrast enhancing lesions (0.20 ± 0.13), areas of edema (0.12 ± 0.05), and necrosis (0.14 ± 0.05). No significant differences between white matter and pathological areas were found for the pseudo-diffusion coefficient, D^* (Table 5). A similar pattern was observed for the IVIM-parameters computed using the fixed-threshold algorithm (Table 5) with the exception of the f_P value that was significantly higher in the lesion than in the reference tissue. Absolute values of IVIM parameters depended on the algorithm used (Fig. 4).

A significant, high to very high negative correlation was found in the pathological areas between $f_{P,variable\text{-}threshold}$ and CBF, while the correlation ranged between negative, moderate and high for $f_{P,fixed\text{-}threshold}$ (Table 4b, Fig. 5). A moderate positive correlation was found between $D^*_{variable\text{-}threshold}$ and CBF in lesions and necrotic tissue, while in the same regions low correlation was measured using the fixed-threshold algorithm. For the variable-threshold algorithm, no correlation was found between CBF and $f_P \cdot D^*$ in any of the pathological regions, while a moderate negative correlation was found between CBF and $f_P \cdot D^*$ estimated using the fixed-threshold algorithm over the contrast-enhancing lesions. Over the pathological areas, there was a low negative correlation between CBF and D.

6. Discussion

In spite of the potential of IVIM in the non-invasive characterization of malignant brain lesions (Bisdas et al., 2014; Federau et al., 2014; Hu et al., 2014; Shim et al., 2015), the use of this model in clinics is hampered by the poor stability of standard IVIM algorithms (Wu et al., 2015) on one side and by the still incomplete interpretation of the IVIM indexes in pathologies (Bisdas et al., 2014; Bisdas and Klose, 2015; Federau et al., 2013; Wirestam et al., 2001) on the other side.

The main results of this study are threefold: (i) accounting for regional differences in the separation of the perfusion and the diffusion components in IVIM improves the repeatability of the model; (ii) if differences in the b-value threshold are not accounted for, a significant tissue-dependent mis-estimation of the IVIM-indexes may occur; (iii) accounting for regional differences in the separation of the perfusion and the diffusion components in IVIM improves the correlation with CBF measurements in the healthy gray matter in volunteers and intracranial lesions.

In this study the investigation of the repeatability of the IVIM measurements in healthy volunteers showed the importance of a local standardized separation of the perfusion and diffusion components. Although no perfusion is expected in the CSF, IVIM algorithms provided

Table 4b
Spearman's correlation coefficients between CBF and IVIM indexes in patients. Statistically significant correlation ($p < 0.05$) is highlighted in bold font.

		Contrast-Enhancing Lesion	Edema	Necrotic Region
Variable-threshold algorithm	CBF vs D	−0.36	−0.46	−0.15
	CBF vs $f_P \cdot D^*$	−0.29	0.00	0.20
	CBF vs f_P	**−0.96**	**−0.89**	**−0.89**
	CBF vs D^*	**0.70**	0.46	0.66
Fixed-threshold algorithm	CBF vs D	−0.46	−0.54	−0.35
	CBF vs $f_P \cdot D^*$	−0.75	−0.18	−0.49
	CBF vs f_P	**−0.89**	−0.61	−0.77
	CBF vs D^*	−0.31	−0.04	0.14

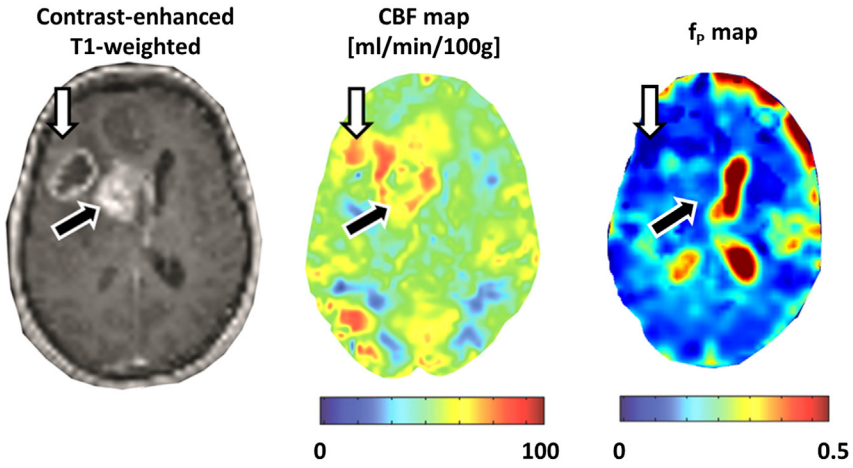

Fig. 5. Cropped parametrical CBF and f_P maps computed in one patient (female, 55 years-old, diagnosis of GBM) are reported. Areas of hyper-perfusion at the border to a ring enhancing lesion (white arrow) correspond to low f_P values. The contrast-enhancing lesion visible in the T1-weighted image (black arrow) was characterized by heterogeneous perfusion and low mean f_P values.

relatively high f_P values of the CSF in the order of 0.25 (Table 2). These high values may result from contamination of CSF flow encoded by the flow-sensitive gradients, similarly to the case of velocity-selective ASL techniques (Wu and Wong, 2004).

The comparison of the mean values reported in this manuscript with literature values is hindered by the dependence of the IVIM-parameters on the selection of the b-value threshold (Fig. 4). For the standard algorithm used in this manuscript a good accordance was found with the literature values reported for white and gray matter (Wu et al., 2015). The variable-threshold algorithm also yielded gray matter values comparable with published values of healthy volunteers (Wu et al., 2015). The accordance with the values reported in the literature, as well as, the results of our study concerning the optimal b-value thresholds for the brain confirm that b-values in the order of 150–250 s/mm^2 are optimal threshold for the gray matter. In this study a b-value of 160 s/mm^2 was used as threshold for the standard algorithm. However, the results of our study show that optimal thresholding for the white matter occurs around 380 s/mm^2. Therefore, we cannot exclude that the signal arising from slow moving capillary spins may have partially affected the estimation of the IVIM parameters using the fixed-threshold algorithm.

Similarly to the case of the healthy tissue, also regional values computed in this study over pathological areas cannot be directly compared to the literature. A positive correlation between CBF and D^* was found using the variable-threshold algorithm in all pathological areas. The fraction of perfusion f_P correlated negatively with CBF in contrast enhancing lesions and the putamen, in accordance with Lin et al. (Lin et al., 2015). These results may be surprising if considering the linear proportionality between the cerebral blood volume and f_P proposed in (Le Bihan and Turner, 1992). However our results are in keeping with the study of Bisdas and colleagues, where measurements of plasma flow with dynamic contrast MRI correlated negatively to the fraction of perfusion and positively with D^* in lesions (Bisdas et al., 2014). The negative correlation between CBF and f_P may reflect the abnormality of the blood flow in lesions due to hyper-permeability of the vessels and variability of vessels thickness (Jain et al., 2007). However, as we detected the same dependency also in the putamen, we speculate that this result may reflect the interdependence between the two IVIM parameters f_P and D^*, which has been reported in other arterially perfused organs as spleen and bowel (Eberhardt et al., 2016). In tissue types which present high capillary blood velocity (e.g. the gray matter (Rosenberg and Kyner, 1980) or brain tissue under hypoxic conditions (Bereczki et al., 1993)) the contribution of the capillary network to the diffusion-weighted MR signal is expected to quickly disappear for low b-values. In this case, if the algorithm is not accounting for a regional adjustment of the b-value threshold, the fraction of perfusion is overestimated and the pseudo-diffusion coefficient is underestimated. The bias will depend on both, the selected threshold and the local capillary blood velocity. In the study from Federau et al. (Federau et al., 2014), a positive correlation between CBV and f was found in tumor lesions. However, the use of an algorithm with 200 s/mm^2 fixed-threshold hinders the direct comparison of the results with our findings.

Few main limitations should be considered in this work. The small number of patients included in the study and the heterogeneity of the cohort of patients do not allow a comprehensive interpretation of the IVIM values in patients. Moreover, although this study aimed to provide mean values for healthy tissue and pathological areas, the heterogeneity of the distribution of the values within specific areas (Fig. 5) may also be an important index for the characterization of the pathological conditions. A third point concerns the issue of the CBF quantification (Eq. 3). The equilibrium magnetization of the brain tissue, M_0, can be estimated from the signal measured on a RoI drawn over the control volume and corrected for T1 decay (Aslan et al., 2010). In this study we opted for the acquisition of a control volume with a long labeling delay. The advantage of that is a pixel wise estimation of the equilibrium magnetization. However, depending on the T1 time of the tissue, local overestimation of the CBF values may have occurred. On the other side, the choice of a relative short post-delay time (Aslan et al., 2010) may have led to a slight underestimation of the CBF. In few volunteers head size and shape resulted in limited areas of inadequate fat suppression of the diffusion-weighted images which may have residually

Table 5
Mean values (± standard deviation) of the IVIM indexes computed using the variable-threshold algorithm and the fixed-threshold algorithm in patients.

	D [10^{-3} mm^2/s]		D^* [10^{-3} mm^2/s]		f_P	
	Variable-threshold	Fixed-threshold	Variable-threshold	Fixed-threshold	Variable-threshold	Fixed-threshold
White matter	0.64 ± 0.05	0.70 ± 0.04	6.4 ± 4.5	7.0 ± 2.0	0.12 ± 0.03	0.08 ± 0.02
Contrast-enhancing lesion	0.88 ± 0.14	0.98 ± 0.18	11.6 ± 9.5	15.6 ± 9.8	0.20 ± 0.13	0.16 ± 0.10
Edema	1.06 ± 0.19	1.12 ± 2.10	19.1 ± 29.3	12.5 ± 13.1	0.12 ± 0.05	0.10 ± 0.05
Necrotic region	0.97 ± 0.24	1.03 ± 0.24	9.9 ± 5.3	6.2 ± 1.8	0.14 ± 0.05	0.11 ± 0.04

contributed to the mean IVIM values. Finally, in this study diffusion-weighted images were acquired without cardiac gating. Federau et al. (Federau et al., 2013) investigated the dependence of the IVIM parameters measured over the whole brain from the cardiac cycle. The systolic pseudo-diffusion coefficient was significantly higher than the one acquired without gating, while no significant changes were found for the diffusion coefficient and the fraction of perfusion. The pulsatility of the microcirculation may affect the quantification of the pseudo-diffusion coefficient. The accuracy of the estimations of the pseudo-diffusion coefficient may improve using cardiac gated acquisitions. However, cardiac gating occurs at costs of acquisition time, and it may be not feasible for clinical use.

In conclusion, the proposed algorithm provides a robust characterization of regional micro-vascularization and cellularity without a priori assumptions on tissue diffusion properties. The glioblastoma multiforme with its inherently high variability of tumor vascularization and tumor cell density may benefit from a non-invasive clinical characterization of diffusion and perfusion properties.

Acknowledgement

This work was supported by the Clinical Research Priority Program (CRPP) Tumor oxygenation of the University of Zurich and by the Foundation for Research at the Faculty of Medicine, University of Zurich (grant no. 34270124). The authors thank Dr. Roger Lüchinger for technical advice, and Dr. Daniel Nanz for carefully proof reading the manuscript.

Appendix A. Supplementary data

Supplementary data to this article can be found online at http://dx.doi.org/10.1016/j.nicl.2016.05.022.

References

Akgoz, A., Rahman, R., You, H., Qu, J., Hamdan, A., Seethamraju, R.T., Wen, P.Y., Young, G.S., 2014. Spin-echo echo-planar perfusion prior to chemoradiation is a strong independent predictor of progression-free and overall survival in newly diagnosed glioblastoma. J. Neuro-Oncol. 119, 111–119.

Ashburner, J., Andersson, J.L., Friston, K.J., 2000. Image registration using a symmetric prior—in three dimensions. Hum. Brain Mapp. 9, 212–225.

Aslan, S., Xu, F., Wang, P.L., Uh, J., Yezhuvath, U.S., van Osch, M., Lu, H., 2010. Estimation of labeling efficiency in pseudocontinuous arterial spin labeling. Magn. Reson. Med. 63, 765–771.

Bereczki, D., Wei, L., Otsuka, T., Acuff, V., Pettigrew, K., Patlak, C., Fenstermacher, J., 1993. Hypoxia increases velocity of blood flow through parenchymal microvascular systems in rat brain. J. Cereb. Blood Flow Metab. 13, 475–486.

Bisdas, S., Klose, U., 2015. IVIM analysis of brain tumors: an investigation of the relaxation effects of CSF, blood, and tumor tissue on the estimated perfusion fraction. MAGMA 28, 377–383.

Bisdas, S., Braun, C., Skardelly, M., Schittenhelm, J., Teo, T.H., Thng, C.H., Klose, U., Koh, T.S., 2014. Correlative assessment of tumor microcirculation using contrast-enhanced perfusion MRI and intravoxel incoherent motion diffusion-weighted MRI: is there a link between them? NMR Biomed. 27, 1184–1191.

Chenevert, T.L., Sundgren, P.C., Ross, B.D., 2006. Diffusion imaging: insight to cell status and cytoarchitecture. Neuroimaging Clin. N. Am. 16, 619–632 (viii–ix).

Cicchetti, D.V., Sparrow, S.A., 1981. Developing criteria for establishing interrater reliability of specific items: applications to assessment of adaptive behavior. Am. J. Ment. Defic. 86, 127–137.

Eberhardt, C., Wurnig, M.C., Wirsching, A., Rossi, C., Rottmar, M., Ozbay, P.S., Filli, L., Lesurtel, M., Boss, A., 2016. Intravoxel incoherent motion analysis of abdominal organs: computation of reference parameters in a large cohort of C57Bl/6 mice and correlation to microvessel density. MAGMA.

Federau, C., Hagmann, P., Maeder, P., Muller, M., Meuli, R., Stuber, M., O'Brien, K., 2013. Dependence of brain intravoxel incoherent motion perfusion parameters on the cardiac cycle. PLoS One 8, e72856.

Federau, C., O'Brien, K., Meuli, R., Hagmann, P., Maeder, P., 2014. Measuring brain perfusion with intravoxel incoherent motion (IVIM): initial clinical experience. J. Magn. Reson. Imaging 39, 624–632.

Freiman, M., Voss, S.D., Mulkern, R.V., Perez-Rossello, J.M., Callahan, M.J., Warfield, S.K., 2012. In vivo assessment of optimal b-value range for perfusion-insensitive apparent diffusion coefficient imaging. Med. Phys. 39, 4832–4839.

Furnari, F.B., Fenton, T., Bachoo, R.M., Mukasa, A., Stommel, J.M., Stegh, A., Hahn, W.C., Ligon, K.L., Louis, D.N., Brennan, C., Chin, L., DePinho, R.A., Cavenee, W.K., 2007. Malignant astrocytic glioma: genetics, biology, and paths to treatment. Genes Dev. 21, 2683–2710.

Hu, Y.C., Yan, L.F., Wu, L., Du, P., Chen, B.Y., Wang, L., Wang, S.M., Han, Y., Tian, Q., Yu, Y., Xu, T.Y., Wang, W., Cui, G.B., 2014. Intravoxel incoherent motion diffusion-weighted MR imaging of gliomas: efficacy in preoperative grading. Sci. Rep. 4, 7208.

Jain, R.K., di Tomaso, E., Duda, D.G., Loeffler, J.S., Sorensen, A.G., Batchelor, T.T., 2007. Angiogenesis in brain tumours. Nat. Rev. Neurosci. 8, 610–622.

Jain, R., Poisson, L.M., Gutman, D., Scarpace, L., Hwang, S.N., Holder, C.A., Wintermark, M., Rao, A., Colen, R.R., Kirby, J., Freymann, J., Jaffe, C.C., Mikkelsen, T., Flanders, A., 2014. Outcome prediction in patients with glioblastoma by using imaging, clinical, and genomic biomarkers: focus on the nonenhancing component of the tumor. Radiology 272, 484–493.

Jarnum, H., Steffensen, E.G., Knutsson, L., Frund, E.T., Simonsen, C.W., Lundbye-Christensen, S., Shankaranarayanan, A., Alsop, D.C., Jensen, F.T., Larsson, E.M., 2010. Perfusion MRI of brain tumours: a comparative study of pseudo-continuous arterial spin labelling and dynamic susceptibility contrast imaging. Neuroradiology 52, 307–317.

Le Bihan, D., 2011. Magnetic resonance diffusion imaging: introduction and concepts. In: Jones, D.K. (Ed.), Diffusion MRI: Theory, Methods, and Applications. University Press, Oxford, pp. 66–69.

Le Bihan, D., Turner, R., 1992. The capillary network: a link between IVIM and classical perfusion. Magn. Reson. Med. 27, 171–178.

Le Bihan, D., Breton, E., Lallemand, D., Aubin, M.L., Vignaud, J., Laval-Jeantet, M., 1988. Separation of diffusion and perfusion in intravoxel incoherent motion MR imaging. Radiology 168, 497–505.

Lemke, A., Stieltjes, B., Schad, L.R., Laun, F.B., 2011. Toward an optimal distribution of b values for intravoxel incoherent motion imaging. Magn. Reson. Imaging 29, 766–776.

Li, J., Wang, M., Won, M., Shaw, E.G., Coughlin, C., Curran Jr., W.J., Mehta, M.P., 2011. Validation and simplification of the radiation therapy oncology group recursive partitioning analysis classification for glioblastoma. Int. J. Radiat. Oncol. Biol. Phys. 81, 623–630.

Lin, Y., Li, J., Zhang, Z., Xu, Q., Zhou, Z., Zhang, Z., Zhang, Y., Zhang, Z., 2015. Comparison of intravoxel incoherent motion diffusion-weighted MR imaging and arterial spin labeling MR imaging in gliomas. BioMed Res. Int. 2015, 234245.

Luciani, A., Vignaud, A., Cavet, M., Nhieu, J.T., Mallat, A., Ruel, L., Laurent, A., Deux, J.F., Brugieres, P., Rahmouni, A., 2008. Liver cirrhosis: intravoxel incoherent motion MR imaging–pilot study. Radiology 249, 891–899.

Paravati, A.J., Heron, D.E., Landsittel, D., Flickinger, J.C., Mintz, A., Chen, Y.F., Huq, M.S., 2011. Radiotherapy and temozolomide for newly diagnosed glioblastoma and anaplastic astrocytoma: validation of radiation therapy oncology group-recursive partitioning analysis in the IMRT and temozolomide era. J. Neuro-Oncol. 104, 339–349.

Parker, N.R., Khong, P., Parkinson, J.F., Howell, V.M., Wheeler, H.R., 2015. Molecular heterogeneity in glioblastoma: potential clinical implications. Front Oncol. 5, 55.

Pazahr, S., Nanz, D., Rossi, C., Chuck, N., Stenger, I., Wurnig, M.C., Schick, F., Boss, A., 2014. Magnetic resonance imaging of the liver: apparent diffusion coefficients from multiexponential analysis of b values greater than 50 s/mm2 do not respond to caloric intake despite increased portal-venous blood flow. Investig. Radiol. 49, 138–146.

Piludu, F., Marzi, S., Pace, A., Villani, V., Fabi, A., Carapella, C.M., Terrenato, I., Antenucci, A., Vidiri, A., 2015. Early biomarkers from dynamic contrast-enhanced magnetic resonance imaging to predict the response to antiangiogenic therapy in high-grade gliomas. Neuroradiology 57, 1269–1280.

Rosenberg, G.A., Kyner, W.T., 1980. Gray and white matter brain-blood transfer constants by steady-state tissue clearance in cat. Brain Res. 193, 59–66.

Shim, W.H., Kim, H.S., Choi, C.G., Kim, S.J., 2015. Comparison of apparent diffusion coefficient and intravoxel incoherent motion for differentiating among glioblastoma, metastasis, and lymphoma focusing on diffusion-related parameter. PLoS One 10, e0134761.

Shrout, P.E., Fleiss, J.L., 1979. Intraclass correlations: uses in assessing rater reliability. Psychol. Bull. 86, 420–428.

Wirestam, R., Borg, M., Brockstedt, S., Lindgren, A., Holtas, S., Stahlberg, F., 2001. Perfusion-related parameters in intravoxel incoherent motion MR imaging compared with CBV and CBF measured by dynamic susceptibility-contrast MR technique. Acta Radiol. 42, 123–128.

Wu, W., Wong, E., 2004. The effects of water diffusion and laminar flow on velocity-selective arterial spin labeling. Conf. Proc. IEEE Eng. Med. Biol. Soc. 3, 1884–1887.

Wu, W.C., Chen, Y.F., Tseng, H.M., Yang, S.C., My, P.C., 2015. Caveat of measuring perfusion indexes using intravoxel incoherent motion magnetic resonance imaging in the human brain. Eur. Radiol. 25, 2485–2492.

Wurnig, M.C., Donati, O.F., Ulbrich, E., Filli, L., Kenkel, D., Thoeny, H.C., Boss, A., 2015. Systematic analysis of the intravoxel incoherent motion threshold separating perfusion and diffusion effects: proposal of a standardized algorithm. Magn. Reson. Med. 74, 1414–1422.

Yamashita, K., Hiwatashi, A., Togao, O., Kikuchi, K., Hatae, R., Yoshimoto, K., Mizoguchi, M., Suzuki, S.O., Yoshiura, T., Honda, H., 2016. MR imaging-based analysis of glioblastoma multiforme: estimation of IDH1 mutation status. AJNR Am. J. Neuroradiol. 37, 58–65.

Yoshiura, T., Hiwatashi, A., Yamashita, K., Ohyagi, Y., Monji, A., Takayama, Y., Nagao, E., Kamano, H., Noguchi, T., Honda, H., 2009. Simultaneous measurement of arterial transit time, arterial blood volume, and cerebral blood flow using arterial spin-labeling in patients with Alzheimer disease. AJNR Am. J. Neuroradiol. 30, 1388–1393.